



SIK2 orchestrates actin-dependent host response upon *Salmonella* infection

Marcel Hahn^a, Adriana Covarrubias-Pinto^a, Lina Herhaus^a, Shankha Satpathy^{b,1}, Kevin Klann^a, Keith B. Boyle^c, Christian Münch^a, Krishnaraj Rajalingam^d, Felix Randow^c, Chunaram Choudhary^b, and Ivan Dikic^{a,e,2}

^aInstitute of Biochemistry II, Goethe University School of Medicine, 60590 Frankfurt am Main, Germany; ^bDepartment of Proteomics, The Novo Nordisk Foundation Center for Protein Research, Faculty of Health and Medical Sciences, University of Copenhagen, Blegdamsvej 3B, Copenhagen 2200, Denmark; ^cDivision of Protein and Nucleic Acid Chemistry, Medical Research Council (MRC) Laboratory of Molecular Biology, CB2 0QH Cambridge, United Kingdom; ^dCell Biology Unit, University Medical Center of the Johannes Gutenberg University Mainz, 55131 Mainz, Germany; and ^eBuchmann Institute for Molecular Life Sciences, Goethe University Frankfurt, 60438 Frankfurt, Germany

Edited by Vishva M. Dixit, Genentech, San Francisco, CA, and approved April 1, 2021 (received for review November 20, 2020)

***Salmonella* is an intracellular pathogen of a substantial global health concern. In order to identify key players involved in *Salmonella* infection, we performed a global host phosphoproteome analysis subsequent to bacterial infection. Thereby, we identified the kinase SIK2 as a central component of the host defense machinery upon *Salmonella* infection. SIK2 depletion favors the escape of bacteria from the *Salmonella*-containing vacuole (SCV) and impairs Xenophagy, resulting in a hyperproliferative phenotype. Mechanistically, SIK2 associates with actin filaments under basal conditions; however, during bacterial infection, SIK2 is recruited to the SCV together with the elements of the actin polymerization machinery (Arp2/3 complex and Formins). Notably, SIK2 depletion results in a severe pathological cellular actin nucleation and polymerization defect upon *Salmonella* infection. We propose that SIK2 controls the formation of a protective SCV actin shield shortly after invasion and orchestrates the actin cytoskeleton architecture in its entirety to control an acute *Salmonella* infection after bacterial invasion.**

Salmonella | actin cytoskeleton | Arp2/3 complex | host–pathogen interactions | *Salmonella*-containing vacuole

S*almonella enterica* is a gram-negative, facultative intracellular human pathogen, annually causing more than 100 million food- and waterborne infections worldwide. *Salmonella* Typhimurium causes severe gastroenteritis, which could turn into a systemic infection in children, immune-compromised, or elderly people (1, 2). Concurrently, multidrug resistant bacteria are globally emerging and threatening our health systems, calling for a better understanding of the underlying virulence mechanism and host response.

Pathogenic bacteria have evolved the inherent ability to infect and to establish their niche within host cells. For colonizing non-phagocytic cells such as epithelial cells, *Salmonella* uses a trigger mechanism–based entry mode. Bacterial virulence factors are then injected via a Type III-secretion system (T3SS) into the host cell to induce cytoskeletal rearrangements leading to membrane ruffling and macropinocytosis-driven internalization into a sealed phagosome (3, 4). This specialized compartment is referred to as the *Salmonella*-containing vacuole (SCV) and serves as the intracellular replicative niche by hiding the bacteria from the humoral and cell-autonomous immune response (5). *Salmonella* invasion requires a cooperative action of several bacterial effector proteins hijacking multiple host targets. One of the main targets forcing *Salmonella*'s uptake is the actin cytoskeleton by subverting the host Rho GTPases system. Bacterial effector proteins such as SopE/SopE2 mimic host nucleotide exchange factors (GEFs) to stimulate Rac1 and CDC42 activity (6, 7). Once GTP-activated, Rho GTPases stimulate downstream pathways to drive actin filament (F-actin) assembly and rearrangement.

The actin cytoskeleton network is regulated by actin-binding proteins (ABPs), which orchestrate assembly and disassembly of actin in higher networks (8). Monomeric, globular actin (G-actin) is nucleated into new actin filaments, or the existing F-actin is

elongated, stabilized, or disassembled by ABPs. The major actin nucleation factor is the multimeric Arp2/3 complex, which generates branched actin filament networks. Formins generate long unbranched actin filaments and represent another actin nucleation family. Together with actin nucleation-promoting factors, small Rho GTPases control ABPs in a spatiotemporal manner. Actin polymerization and membrane ruffling are necessary for *Salmonella* invasion. Following *Salmonella* internalization, the SCV undergoes SPI-1–dependent biogenesis and is transported to a juxtanuclear position at 1 to 2 h postinfection (pi). At later time-points (4 to 6 h pi), SPI-2–dependent effector proteins are expressed to further mature the SCV, allowing bacterial proliferation. Pioneering work described that, at later stages of the infection (≥ 6 h pi), an actin meshwork around the SCV stabilizes and protects the vacuolar niche (9–13).

Here, we report SIK2 as a *Salmonella* resistance factor and a regulator of the actin cytoskeleton. SIK2 belongs to the AMPK kinase family and was named after its homolog SIK1, found to be expressed upon high-salt diet-induced stress in rats (14, 15). SIK2 has been implicated into multiple biological roles including melanogenesis, cancer progression, and gluconeogenesis (16–18). SIK2 depletion results in a loss of SCV integrity and bacterial escape into the host cytosol, causing intracellular *Salmonella* hyperproliferation. Notably, SIK2 depletion results in a severe pathological cellular

Significance

Through conducting quantitative proteomics upon *Salmonella* infection, we identified a SIK2 signaling network, implementing the kinase into a so far concealed biological function. Our data exposed SIK2 as a central orchestrator of an actin regulatory network, coordinating the stability of *Salmonella*-containing vacuole (SCV) and cellular actin assembly, in order to limit the acute phase of the infection. Most strikingly, SIK2 is not exclusively acting locally on actin assembly associated with the SCV but impacts the actin cytoskeleton architecture in its entirety upon *Salmonella* infection. Our work provides a mechanistic framework for how the actin cytoskeleton is regulated and how it helps to control an acute *Salmonella* infection.

Author contributions: M.H. and I.D. designed research; M.H., A.C.-P., L.H., and S.S. performed research; K.B.B., K.R., and F.R. contributed new reagents/analytic tools; M.H., S.S., K.K., C.M., and C.C. analyzed data; and M.H. and I.D. wrote the paper.

The authors declare no competing interest.

This article is a PNAS Direct Submission.

This open access article is distributed under [Creative Commons Attribution-NonCommercial-NoDerivatives License 4.0 \(CC BY-NC-ND\)](https://creativecommons.org/licenses/by-nc-nd/4.0/).

¹Present address: Broad Proteomics, Broad Institute of Massachusetts Institute of Technology and Harvard, Cambridge, MA 02142.

²To whom correspondence may be addressed. Email: dikic@biochem2.uni-frankfurt.de.

This article contains supporting information online at <https://www.pnas.org/lookup/suppl/doi:10.1073/pnas.2024144118/-DCSupplemental>.

Published May 4, 2021.

actin nucleation and polymerization defect upon *Salmonella* infection. Hence, SIK2 may represent a cellular safeguard, which controls the actin cytoskeleton and SCV integrity, thereby serving as a prime regulator of *Salmonella* proliferation subsequent to cellular internalization.

Results

Quantitative Phosphoproteomics in *Salmonella*-Infected Epithelial Cells. In order to shed light on the signaling pathways underlying the *Salmonella* infection, we performed quantitative phosphoproteomics. HCT116 cells were metabolically labeled with stable isotope labeling of amino acid in cell culture (SILAC), allowing the relative quantification of peptides by high-resolution mass spectrometry (MS). To this end, we used a triple-SILAC labeling in which “light”-labeled cells were left uninfected and “heavy”- and “medium”-labeled cells were infected with *Salmonella* and subsequently analyzed (30 min or 2 h pi) (Fig. 1A). In total, we quantified around 17,900 phosphosites from 4,200 proteins that were modified in minimum two out of four experimental replicates. At 30 min pi, the up-regulation of phosphorylation events was most pronounced (Fig. 1B and C). Across all experimental replicates, we mapped 964 phosphosites displaying \log_2 (heavy:light) ratios of ≥ 0.58 indicating a 1.5-fold increase; 626 proteins and 742 phosphosites with \log_2 (heavy:light) ratios of ≤ 0.58 indicating a 1.5-fold decrease; and 481 proteins at 30 min pi (Fig. 1B). Significant \log_2 values represent a P value of ≤ 0.05 . To obtain a general understanding of the host phosphoproteome changes upon *Salmonella* infection, we standardized the data set (z -score) and displayed relative changes of phosphopeptides in a heatmap (Fig. 1D). Our data indicates an acute modulation of phosphorylation events in various signaling pathways shortly after a *Salmonella* infection (Fig. 1E). Pathway analyses of the up-regulated functional interaction network 30 min pi revealed extensive remodeling of Rho

GTPases, like CDC42- and/or Rac1-signaling (Fig. 1E). Among these, we identified over 20 proteins belonging to the Rho GTPase network (e.g., ARHGAP5 and ARHGEF2/11/12), confirming this distinct signaling network as a major target of *Salmonella* at early time points pi (19, 20). An additional functional analysis exhibited a direct association between bacterial invasion and the Rho GTPase pathway as a major cluster in our phosphoproteome data set (SI Appendix, Fig. S1A). Members of tumor necrosis factor (TNF)- and nucleotide-binding oligomerization domain (NOD)-like receptor signaling were also overrepresented pi (Fig. 1E) (SI Appendix, Fig. S1A). Among them were several components of the MAPK/IKK-pathway, followed by pattern recognition receptor activation. We validated the key phosphosites of these pathways using phospho-specific antibodies against components of the MAPK-signaling cascade (SI Appendix, Fig. S1B and C). NOD-like receptors are intracellular PRRs, which recognize bacterial peptidoglycan and SopE-mediated Rho GTPase activation and represent one of the main proinflammatory pathways activated by *Salmonella* infection (21, 22). Our MS data confirm previously published results, indicating that NF- κ B-signaling sets a proinflammatory state to dampen bacterial proliferation in host cells (23).

SIK2 Signaling Network Is Triggered upon *Salmonella* Infection. Analyzing the reproducible and significantly regulated phosphorylation sites 30 min pi, we identified and confirmed the innate immunity kinase TAK1 (MAP3K7) as a central target of *Salmonella*-induced phosphosite modulation (24, 25). Strikingly, we identified the AMPK-related kinase SIK2 as a target of potential similar importance (Fig. 1F). We found SIK2 to be phosphorylated at S117, which represents a phosphorylation site within the kinase domain. Since AMPK-related kinases are poorly characterized and SIK2 has not yet been associated with *Salmonella* infection, we focused on the

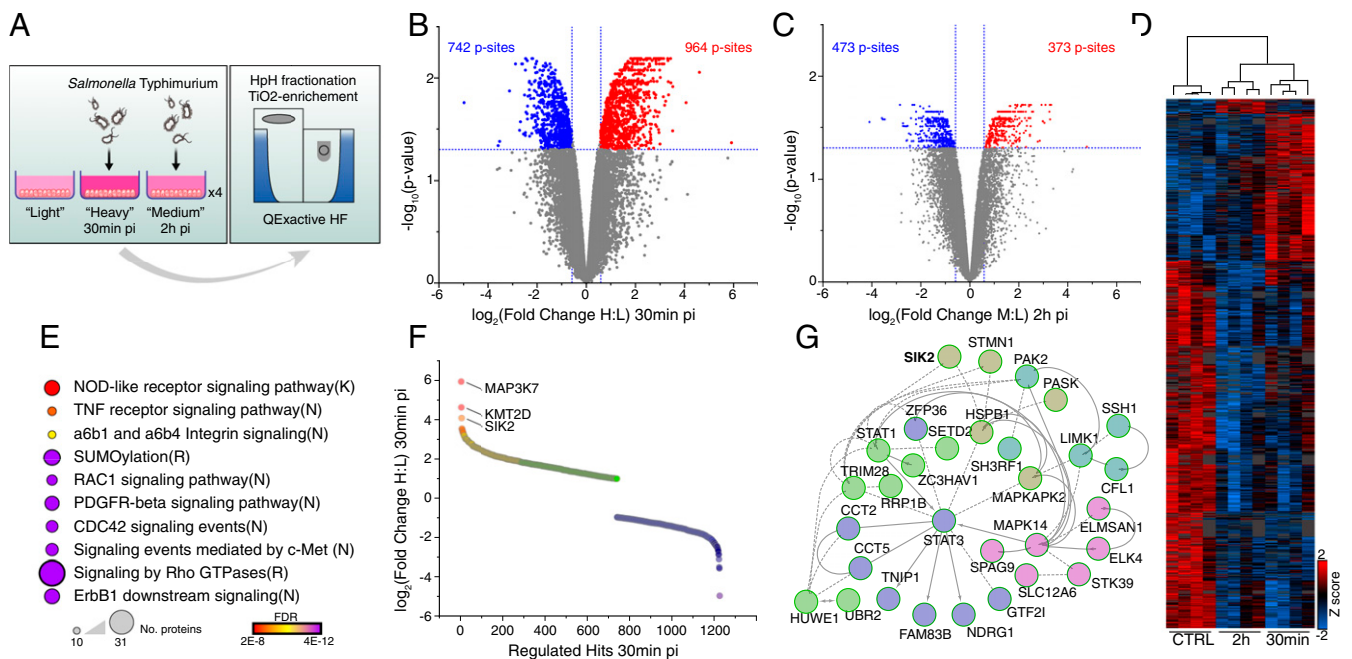


Fig. 1. Global host phosphoproteome reveals SIK2 signaling network upon *Salmonella* infection. (A) The phosphoproteome workflow for 30 min and 2 h pi ($n = 4$). (B) Volcano plot showing relative phosphorylation changes 30 min pi versus noninfected. \log_2 ratios were plotted against $-\log_{10} P$ values. (C) Volcano plot showing relative phosphorylation changes 2 h pi versus noninfected. \log_2 ratios were plotted against $-\log_{10} P$ values. (D) Heatmap and hierarchical clustering summarizing results from Fig. 1A. Z-Scores were calculated and hierarchical clustering performed using Euclidean distance between the samples. Only ANOVA-significant peptides were used (P value ≤ 0.05). (E) Reactome pathway analysis of proteins with up-regulated phospho-sites 30 min pi ($\log_2 \geq 1$ and P value ≤ 0.05). Pathway results are shown with the number of proteins found in dataset and computed FDR for pathway enrichment (FDR < 0.001). (F) Scatter plot showing regulated phosphosites ($\log_2 \leq 1$ or ≥ 1 and P value ≤ 0.05) from 30 min pi. (G) Reactome FI-based SIK2-associated cluster analysis. Up-regulated hits from 30 min pi were FI annotated, clustered, and SIK2-associated cluster isolated.

SIK2-associated functional network in the same dataset (Fig. 1G). In this cluster, we identified several constituents of the Rac1-signaling network (Cofilin-1, PAK2, LIMK1, STAT3, and p38a) (Fig. 1G) (SI Appendix, Fig. S1D). Rac1-signaling is one of the major pathways targeted by SPI-1 *Salmonella* effector proteins to establish an intracellular niche within the host cell, enabling protected proliferation of bacteria (6, 7). This prompted us to further investigate the role of SIK2 during *Salmonella* infection.

SIK2 Is Essential for Restriction of Intracellular *Salmonella* Proliferation.

To test whether SIK2 is required for antibacterial defense in epithelial cells, we used short interfering RNAs (siRNA) to deplete cells of SIK2 (SI Appendix, Fig. S2A). Cells lacking SIK2 failed to restrict proliferation of bacteria within the SCV (Fig. 2A). This phenotype was characterized by bacterial hyperproliferation rather than bacterial hyper-invasion (Fig. 2B). The hyperproliferation of intracellular *Salmonella* was already evident at 6 h pi and increased further at 8 h pi. The phenotype was confirmed by an alternative second siRNA targeting SIK2, which depletes SIK2 protein levels as well (SI Appendix, Fig. S2B). To further characterize the phenotype, we generated a functional HA-SIK2 doxycycline-inducible HeLa cell line, resistant to anti-SIK2 siRNAs. To obtain SIK2

expression levels mimicking endogenous levels, we titrated the doxycycline concentration (SI Appendix, Fig. S2C). Using a low concentration of doxycycline, we observed a full phenotypic rescue by re-expressing SIK2 wild-type levels (Fig. 2C). Thus, wild-type SIK2 controls *Salmonella* infection and functions as a central host defense kinase. Next, we investigated whether besides SIK2 expression, SIK2 kinase activity is required for restricting *Salmonella* proliferation. To this end, we generated a HeLa cell line expressing an inducible and SIK2-siRNA-resistant kinase-inactive (K49A) HA-SIK2. Again, we titrated the doxycycline concentration to mimic endogenous protein levels (SI Appendix, Fig. S2D). Expression of the kinase-inactive mutant failed to restrict bacterial proliferation (Fig. 2D). Therefore, the kinase activity of SIK2 is mandatory to limit bacterial proliferation during an acute infection. By using Phos-Tag gels, we were able to validate the phosphorylation of SIK2 directly following bacterial infection at 15 min pi and at 30 min at endogenous levels (SI Appendix, Fig. S2E and F). The phosphorylation of SIK2 appeared independent of its kinase activity, suggesting a transphosphorylation event of SIK2 by an unidentified up-stream kinase, which was not investigated further (SI Appendix, Fig. S2E). Notably, we observed at 2 h pi an increase in the phosphorylation status of the wild-type kinase, in contrast to

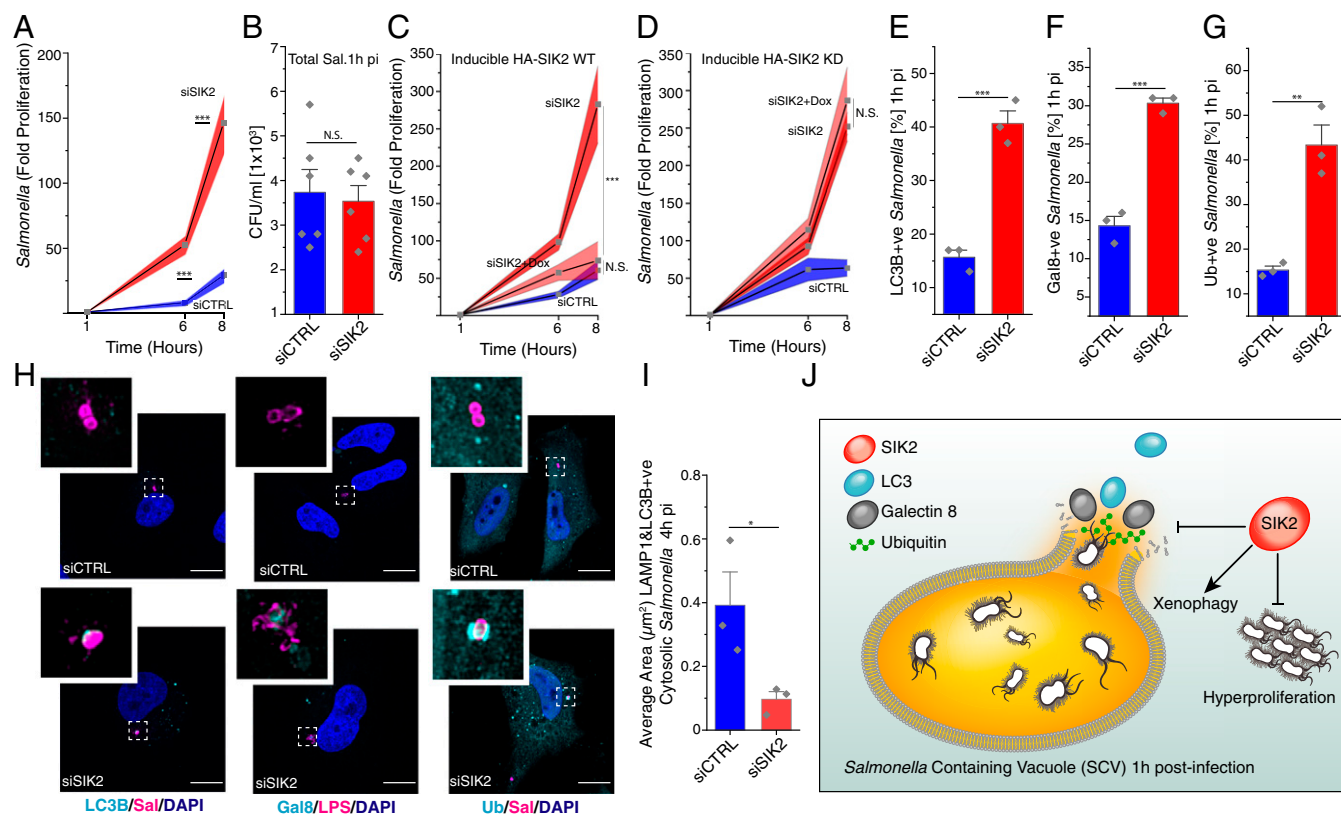


Fig. 2. SIK2 is essential for restriction of intracellular *Salmonella* proliferation. (A) Kinetics of intracellular *Salmonella* replication in HeLa cells. (B) *Salmonella* burden at 1 h pi in HeLa cells. Data are depicted as total CFU/mL at 1 h pi and presented as means + SEM, $n = 3$. (C) Kinetics of intracellular *Salmonella* replication in HeLa cells expressing HA-SIK2 wild type under a doxycycline-inducible promoter. (D) Kinetics of intracellular *Salmonella* replication in HeLa cells expressing HA-SIK2 kinase-deficient (K49A) under a doxycycline-inducible promoter. (E) Quantification of LC3B-positive *Salmonella* from Fig. 2H. (F) Quantification of Galectine8-positive *Salmonella* from Fig. 2H. (G) Quantification of Ubiquitin-positive *Salmonella* from Fig. 2H. (H) Immunofluorescence of siRNA-transfected and *Salmonella*-infected HeLa cells 1 h pi. Cells were stained for endogenous LC3B or Galectine8 or Ubiquitin (ubiquitin FK2 antibody), *Salmonella* (anti-*Salmonella* common structural antigens (CSA) or anti-*Salmonella* lipopolysaccharides (LPS) antibody) and DAPI. Images are maximum intensity projections of confocal z-stacks. (Scale bar, 10 μm.) (I) HeLa cells were siRNA transfected and infected with *Salmonella* SFH2 4 h pi. Cells were stained for LC3B and LAMP1. Average area (micrometers squared) of colocalization of both markers on cytosolic (GFP+ve) *Salmonella* was quantified. (J) Model of observed SIK2 depletion phenotype in HeLa cells 1 h pi. SIK2 depletion results in loss of SCV integrity and favors bacterial escape from the vacuole into the host cytosol, resulting into *Salmonella* hyperproliferation. (A–D) Bacteria were counted on the basis of their ability to form colonies on agar plates. (A, C, and D) Data are depicted as fold proliferation normalized to 1 h pi and presented as means ± SD, $n = 3$, and $***P \leq 0.001$ as analyzed by Student's *t* test. (E–G and J) Data presented as mean + SEM, $n = 3$, >100 bacterial counts per condition, $***P \leq 0.001$, $**P \leq 0.01$, and $*P \leq 0.05$ as analyzed by Student's *t* test. (C and D) Gene expression was induced with 100 ng/mL doxycycline for 24 h preinfection. (A–I) Cells were transfected with nontargeting control- and anti-SIK2 siRNA.

the kinase-inactive version, indicating a cis-phosphorylation (*SI Appendix, Fig. S2E*). By using a SPI-1 deletion *Salmonella* strain, we showed that the phosphorylation depends on SPI-1 effector proteins (*SI Appendix, Fig. S2F*). To further investigate SIK2 phosphorylation, we made use of GFP-SopA- and GFP-SopE-inducible HeLa cell lines to test whether these SPI-1 effector proteins mediate SIK2 activation (*SI Appendix, Fig. S2G*). Our data indicates that SIK2 is being phosphorylated in a SopE-dependent manner and activated further during the early phase of a *Salmonella* infection.

SIK2 Controls SCV Integrity and Bacterial Evasion. To understand the SIK2 depletion phenotype, we studied the fate of intracellular bacteria using confocal microscopy. The autophagy modifier LC3B selectively targets autophagic cargo (such as bacteria) to the autophagosome to promote its autophagic degradation. Therefore, we monitored endogenous LC3B recruitment to *Salmonella* 1 h pi. In accordance with literature (26), siCTRL-transfected cells showed an LC3B-*Salmonella* colocalization rate of ~15%. In contrast, cells depleted of SIK2 showed a significantly higher percentage of LC3B-positive *Salmonella* (close to 40%) (Fig. 2 E and H). Using Galectin-8 as a marker of vesicle, endosomal, or lysosomal integrity revealed a significant increase in Galectin-8-positive *Salmonella* after depleting SIK2 from cells (Fig. 2 F and H). Using ubiquitin as an alternative damage marker, we confirmed this finding (Fig. 2 G and H). Thus, SIK2 depletion causes SCV damage, enabling enhanced bacterial access to the host cytosol. To study the fate of cytosolic bacteria, we used a *Salmonella* strain expressing green fluorescent protein (GFP) only, when exposed to the host cytosol, controlled by a glucose-6-phosphate-inducible promoter (27). By studying endogenous LC3B and LAMP1 recruitment at 4 h pi, we found significant less colocalization of both markers on cytosolic bacteria after SIK2 depletion (Fig. 2I). SIK2 ensures the integrity of the SCV, thus preventing *Salmonella* from entering the host cytosol in HeLa cells, in which bacterial hyperproliferation occurs (28). Furthermore, SIK2 is required for autolysosome formation and therefore for the degradation of cytosolic bacteria via the autophagy-lysosomal system (Fig. 2J).

Recruitment of SIK2 upon Infection to Actin Cytoskeleton Network.

To understand the role of SIK2 during the course of a *Salmonella* infection, we tagged endogenous SIK2 with an HA tag at its C terminus in a HeLa cell line, using CRISPR/Cas12-assisted PCR-tagging (29). This cell line was used for immunoprecipitation and subsequent quantitative TMT-based mass spectrometry (IP-MS) (Fig. 3A). Under basal, noninfected conditions we were able to identify 21 significant interaction partners of SIK2, which fulfilled our stringent criteria (Fig. 3B). As expected, the bait SIK2 was the most enriched protein. Among the SIK2-interacting partners were the Rho GTPase CDC42, ACTBL2 encoding kappa-actin, CLTB/Clathrin light chain B, TPM2/Tropomyosin-beta, MYL3/Myosin light chain 3, and CORO1C/Coronin-1C, pointing toward a potential role in the basal cytoskeleton dynamics (Fig. 3B). Upon *Salmonella* infection, the SIK2 interactome profile changed to a much higher degree of complexity, and we observed 175 cointeracting partners of SIK2. This indicates that SIK2 is recruited to a larger protein interactome at 1 h pi (Fig. 3C). To rule out technical reasons for this increased complexity, we plotted the fold-changes of uninfected versus infected samples on a scatter plot. Our data demonstrated equal immunoprecipitation of SIK2 in both settings and a pronounced shift in the interactome triggered by *Salmonella* infection (*SI Appendix, Fig. S3C*). Functional pathway analysis of the SIK2 interactome upon infection revealed strong enrichment of bacterial/*Salmonella* infection pathway components, such as Rho GTPases and the regulation of the actin cytoskeleton (Fig. 3D) (*SI Appendix, Fig. S3A*). The hits from both categories were clustered hierarchically, revealing that SIK2 is interacting with the entire Arp2/3 complex (Arp2/ACTR2, Arp3/ACTR3, p41/ARPC1A&B,

p34/ARPC2, p21/ARPC3, p20/ARPC4, and p16/ARPC5) and additional known modulators of this complex, such as CDC42, CTTN/Cortactin, and IQGAP1 (Fig. 3E) (*SI Appendix, Fig. S3B*) (30). Arp2/3 complex represents the main F-actin nucleation factor generating branched actin networks (31, 32). We also identified the Formin FMNL2 as another actin nucleation factor, required for linear actin polymerization (33). Additionally, several factors encoding type II myosin like MYH9, MYH11, MYH14, and molecular constituents involved in actin stress fiber formation (e.g., ACTN1&4/ α -actinin, FLNA/Filamin-A, CALD1/Caldesmon and Tropomyosin) were identified (Fig. 3E) (*SI Appendix, Fig. S3A and B*) (34). Together with F-actin bundles, myosins form actin stress fibers, which are stabilized by α -actinin (35).

Functional pathway analysis revealed SIK2 recruitment to well-known *Salmonella* targets, such as the Arp2/3 complex, Filamin-A, or type II myosin (MYH9 and MYH10), forming the basis for functional categorization, such as “*Salmonella* infection (K)” (Fig. 3D) (*SI Appendix, Fig. S3A*). Upon *Salmonella* infection, SIK2 is recruited to a central actin hub and to a large number of essential factors for *Salmonella* colonization within the host cell (36, 37). To verify the IP-MS results, we used the same set-up as described before and performed a hemagglutinin (HA) immunoprecipitation (IP), followed by sodium dodecyl sulphate-polyacrylamide gel electrophoresis (SDS-PAGE) and Western blot. We were able to confirm the *Salmonella*-dependent recruitment of SIK2 to actin, cortactin, and the Arp2/3 complex (ARPC2) under endogenous settings (Fig. 3F). In additional IP results, we demonstrated the interaction of SIK2 with FMNL2 and actin under basal, noninfected conditions.

Impact of SIK2 on the Actin Cytoskeleton during Infection. Since the SIK2 kinase activity is required to rescue the siRNA-mediated hyperproliferative phenotype, we explored pathways/networks regulated by SIK2 upon *Salmonella* infection. To this end, we established a SIK2-dependent TMT-based phosphoproteome screen in HeLa cells, in which siRNA-transfected cells were lysed at 30 min pi. Extracted proteins were digested, TMT 16-plexed and used for iron-nitrilotriacetic acid complex (Fe-NTA) phosphopeptide enrichment (Fig. 4A). A principal component analysis (PCA) showed clustering of the respective replicates, which was further analyzed by a Pearson-based column correlation (*SI Appendix, Fig. S4A and B*). To illustrate changes in the phosphoproteome under basal and infection conditions, we calculated z-scores and hierarchically clustered the ANOVA-significant phosphopeptides fulfilling our stringency criteria (Fig. 4B). The data showed a strong effect of SIK2 depletion in the global phosphoproteome, as already evident in the PCA (*SI Appendix, Fig. S4A*). Since the endogenous SIK2 interactome already revealed significant changes upon *Salmonella* infection, we were looking for an infection- and SIK2-dependent cluster in the phosphoproteome (Fig. 4B). Cluster I identifies peptides exhibiting reduced phosphorylation status, whereas cluster II exhibits those with an increased phosphorylation status upon *Salmonella* infection after SIK2 depletion. The overall cluster profile, however, did not change and was not significantly different from control settings (*SI Appendix, Fig. S4C*). To understand the infection-induced phosphorylation events, we performed a functional pathways cluster analysis (Fig. 4C). Most strikingly, the second most pronounced functional cluster was composed of a major fraction of genes regulating the actin cytoskeleton, which runs in parallel to the cluster “signaling by RhoGTPases (R)” (Fig. 4C). Given the background of the endogenous, infection-triggered SIK2 interactome, we filtered cluster I and II to identify all cytoskeleton components. From this information we were able to construct a dense protein-protein network centered around the cytoskeleton elements (Fig. 4D). To narrow down the impact of SIK2 on the cytoskeleton, we calculated the intersection between phosphoproteome clusters I and II and the endogenous SIK2 interactome at 1 h pi (Fig. 4E). Notably, almost one-third of the whole interactome

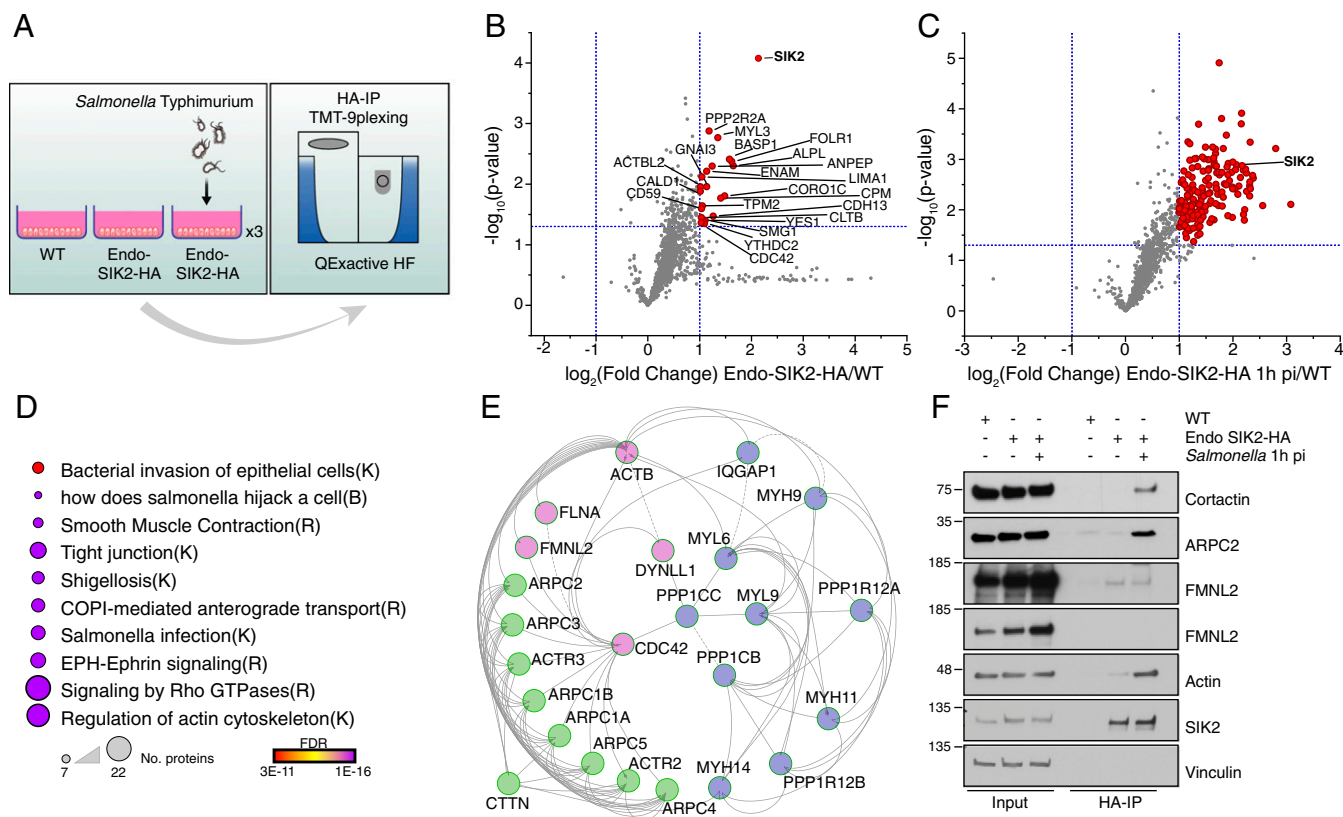


Fig. 3. Recruitment of SIK2 upon infection to an actin cytoskeleton hub. (A) The endogenously tagged SIK2-HA IP workflow. HeLa wild-type or endogenous SIK2-HA-tagged HeLa cells were left uninfected or infected with *Salmonella* and analyzed 1 h pi ($n = 3$). (B) Volcano plot showing relative interaction partners between HeLa endogenous SIK2-HA versus HeLa wild type. Log₂ ratios were plotted against $-\log_{10} P$ values. (C) Volcano plot showing relative interaction partners between HeLa endogenous SIK2-HA infected with *Salmonella* 1 h pi versus HeLa wild type. Log₂ ratios were plotted against $-\log_{10} P$ values. (D) Reactome pathway analysis of regulated interactome of endogenous SIK2-HA upon infection at 1 h pi ($\log_2 \geq 1$ and P value ≤ 0.05). Pathway results are shown with number of proteins found in dataset and computed FDR for pathway enrichment (FDR < 0.001). (E) Reactome FI-based cluster analysis. Endogenous SIK2-HA-interacting partners upon infection at 1 h pi were FI annotated, clustered, and pathway analyzed (q -value < 0.001). The most prominent pathway (from Fig. 3D: signaling by Rho GTPases [R]) was filtered and hierarchically clustered. (F) Endogenous SIK2-HA IP followed by SDS-PAGE and Western blotting. Lysates were probed with the indicates antibodies.

could be assigned to these phosphoproteome clusters. The cytoskeleton-associated intersection was then clustered hierarchically (Fig. 4F). These proteins showed a significantly altered phosphorylation pattern compared to control infection settings. Among these proteins, we found a cluster of proteins required for building up and stabilizing F-actin, including lamellipodia and stress fibers (e.g., ACTN4, FLNA, FNLB, ARPC1B, CTTN, MYO9, MYO10, CALD1/Caldesmon, EMD/Emerin, PDLIM1/Elfin, and LIMA1/EPLIN). Taken together, we identified a SIK2-interacting, actin cytoskeleton-centered network, which shows pronounced changes in the phosphorylation pattern upon SIK2 depletion and *Salmonella* infection.

Endogenous SIK2 Is Colocalized with Actin Filaments and the SCVs. To validate MS and biochemical data, we performed microscopic analysis of cells (MEFs) with a focus on endogenous localization of SIK2 (Fig. 3 E and F). SIK2 showed a localization in the cell periphery, forming foci with a linear arrangement (Fig. 5A). By costaining with Phalloidin, we found SIK2 to colocalize with F-actin-rich regions in MEFs. Thereby, SIK2 decorates polymerized actin fibers with distinct SIK2 foci in MEFs (Fig. 5A). The data showed SIK2 colocalizes with F-actin within the areas undergoing pronounced remodeling and/or de-novo assembly of the actin cytoskeleton under basal, noninfected conditions (Fig. 5 A and B). This finding raised the questions of the localization of SIK2 under an infection scenario. Therefore, we infected MEFs

with *Salmonella* and stained for endogenous SIK2. Most strikingly, we found SIK2 to be recruited to *Salmonella* at 30 min pi, decorating the SCV (Fig. 5B) (SI Appendix, Fig. S5 A and B). The endogenous SIK2 localization was verified by two different anti-SIK2 antibodies (Fig. 5B) (SI Appendix, Fig. S5A). Quantitative analysis showed that more than 50% of the intracellular *Salmonella* colocalized with SIK2 at early time-points pi (SI Appendix, Fig. S5C). The SIK2 interactome revealed interactions with actin nucleation factors such as the Arp2/3 complex or well-established modulators of this complex, such as cortactin. Accordingly, we were able to show by microscopic analysis that these factors also colocalized with the SCV (SI Appendix, Fig. S5 D and E). This is in accordance with SIK2 being recruited to the SCV directly after cellular invasion and corecruitment to the actin network.

SIK2 Impacts Actin Nucleation and Polymerization during *Salmonella* Infection. To address the role of SIK2 in regulating the actin cytoskeleton, we depleted SIK2 by an siRNA approach in HeLa cells and stained for F-actin using Phalloidin. Under noninfected conditions, changes in the structure of the actin cytoskeleton compared to control cells are readily visible (SI Appendix, Fig. S5F). In contrast, after *Salmonella* infection, we observed significantly less F-actin in SIK2-depleted cells, suggesting a breakdown of actin polymerization upon infection (SI Appendix, Fig. S5G). Overall, cortical actin structures and actin stress fibers were dramatically reduced in SIK2-depleted cells; however, the

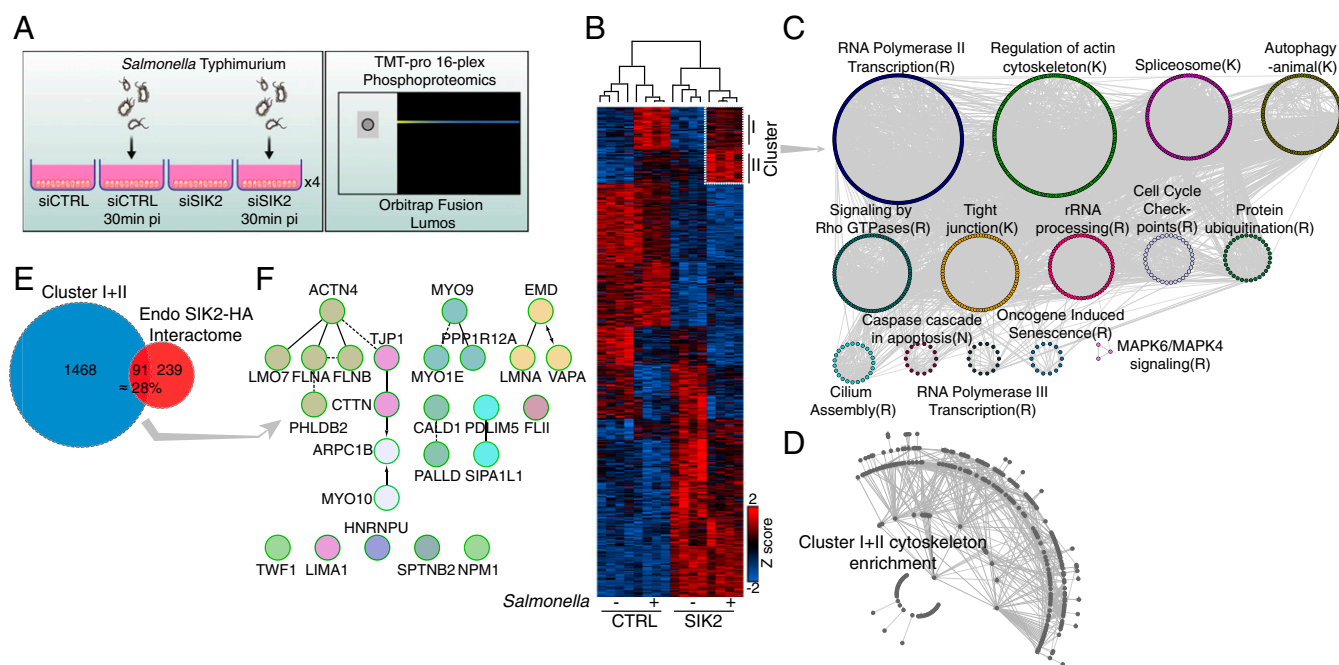


Fig. 4. Impact of SIK2 on the actin cytoskeleton during infection. (A) SIK2-dependent phosphoproteomics workflow ($n = 4$). (B) Heatmap and hierarchical clustering summarizing results from Fig. 4A. Z-scores were calculated and hierarchical clustering performed using Euclidean distance between the samples. Only ANOVA-significant peptides were used (P value ≤ 0.05). (C) ReactomeFl cluster analysis of proteins isolated from cluster I and II. Proteins were Fl annotated, clustered, and clusters analyzed for significantly enriched Reactome pathways (q -value < 0.001). A representative pathway of each cluster is indicated. Connecting lines show interaction of protein nodes. (D) STRING network analysis of proteins from cluster I and II. Network was filtered using cytoskeleton compartment filter (filter set to 3.0) in STRING and clustered. (E) Venn diagram of phosphoproteome cluster I and II and regulated interacting proteins from the endogenous SIK2-HA interactome upon infection ($\log_2 \geq 0.5$ and P value ≤ 0.05). (F) Intersection of Fig. 4E was loaded into STRING and filtered using cytoskeleton compartment filter (filter set to 3.0) and clustered.

microtubules (visualized by tubulin staining) remained unaffected (*SI Appendix, Fig. S5H*). To corroborate the observed defects in actin polymerization, we were able to mimic the microscopic phenotype of SIK2 depletion after *Salmonella* infection by using $2 \mu\text{M}$ of the actin polymerization inhibitor Cytochalasin B for 30 min (*SI Appendix, Fig. S5I*). Using a confocal microscopic quantitative image cytometer platform and subsequent automated analysis, we were able to validate these findings (Fig. 5C). Further biochemical analysis by separating G- and F-actin showed higher levels of G-actin after SIK2 depletion in cells (*SI Appendix, Fig. S5J*). This indicates that SIK2 depletion under basal conditions and particularly in combination with *Salmonella* infection phenocopies a strong actin nucleation and polymerization defect. By using the inducible HA-SIK2 HeLa cell line, resistant to SIK2 siRNAs, we tested whether we can phenotypically rescue the actin polymerization defect upon *Salmonella* infection. In accordance with the *Salmonella* proliferation assay, we were only able to phenotypically rescue actin polymerization with HA-SIK2 wild type, whereas the kinase inactive mutant failed to rescue the phenotype (Fig. 5D). Thus, SIK2 kinase activity is controlling F-actin formation and rearrangements. Overall, our data show that SIK2 is an actin cytoskeleton-modulating effector protein, which is activated upon *Salmonella* infection and recruited to the actin hub centered around the Arp2/3 complex to control F-actin formation in the cell and especially around the SCV in an early phase of *Salmonella* infection.

Discussion

The actin cytoskeleton is central to cell-autonomous immunity during bacterial infections (22). In the present study, we identified a role of SIK2 as a host-defense kinase, regulating the actin cytoskeleton upon *Salmonella* entry into the host cell and restricting the intra-SCV proliferation of *Salmonella*. Our data from cell systems,

working at the endogenous protein levels, indicate that SIK2 represents a central orchestrator of the actin regulatory network, coordinating SCV stability and cellular actin assembly, in order to limit the acute phase of the infection.

To gain access into epithelial cells, *Salmonella* injects effector proteins via its T3SS to modulate the host cytoskeleton by inducing membrane ruffling, resulting in bacterial uptake. SopE and SopE2 are central to *Salmonella*-induced activation of Rac1 and CDC42 by molecularly mimicking host GEFs (7, 38). In addition, SopB, a phosphoinositide phosphatase, is essential for *Salmonella* invasion and activation of RhoG (20). Activated Rac1 and CDC42 recruit the WAVE-regulatory complex to induce the Arp2/3 complex-dependent F-actin polymerization (39, 40). Notably, two *Salmonella* effectors (SipA and SipC) are direct actin-binding proteins, which results in the nucleation and bundling of the actin filaments (41, 42). To ensure spatiotemporal actin rearrangements, *Salmonella* reverses the effects of SopE via the GTPase-activating protein (GAP) SptP, thus normalizing the actin cytoskeleton (43). This study identifies SIK2 as an actin effector protein, controlling F-actin polymerization and limiting the intracellular proliferation of bacteria by restricting it to the SCV. We show that SopE mediates SIK2 phosphorylation and activation. However, it remains unknown how SopE exactly activates SIK2, probably through the exploitation of another host kinase. Given the high similarity with SopE, it is certainly possible that SopE2 might as well trigger SIK2 phosphorylation. Both effector proteins activate directly Rac1 and CDC42, although with different GEF activities and stimulate p21-activated kinase (PAK) signaling, which might be upstream of SIK2 activation.

During a *Salmonella* infection, the SIK2 interactome profile dramatically changes and recruits SIK2 to a dense actin-regulating network, centered around CDC42, the Arp2/3 complex, and actin

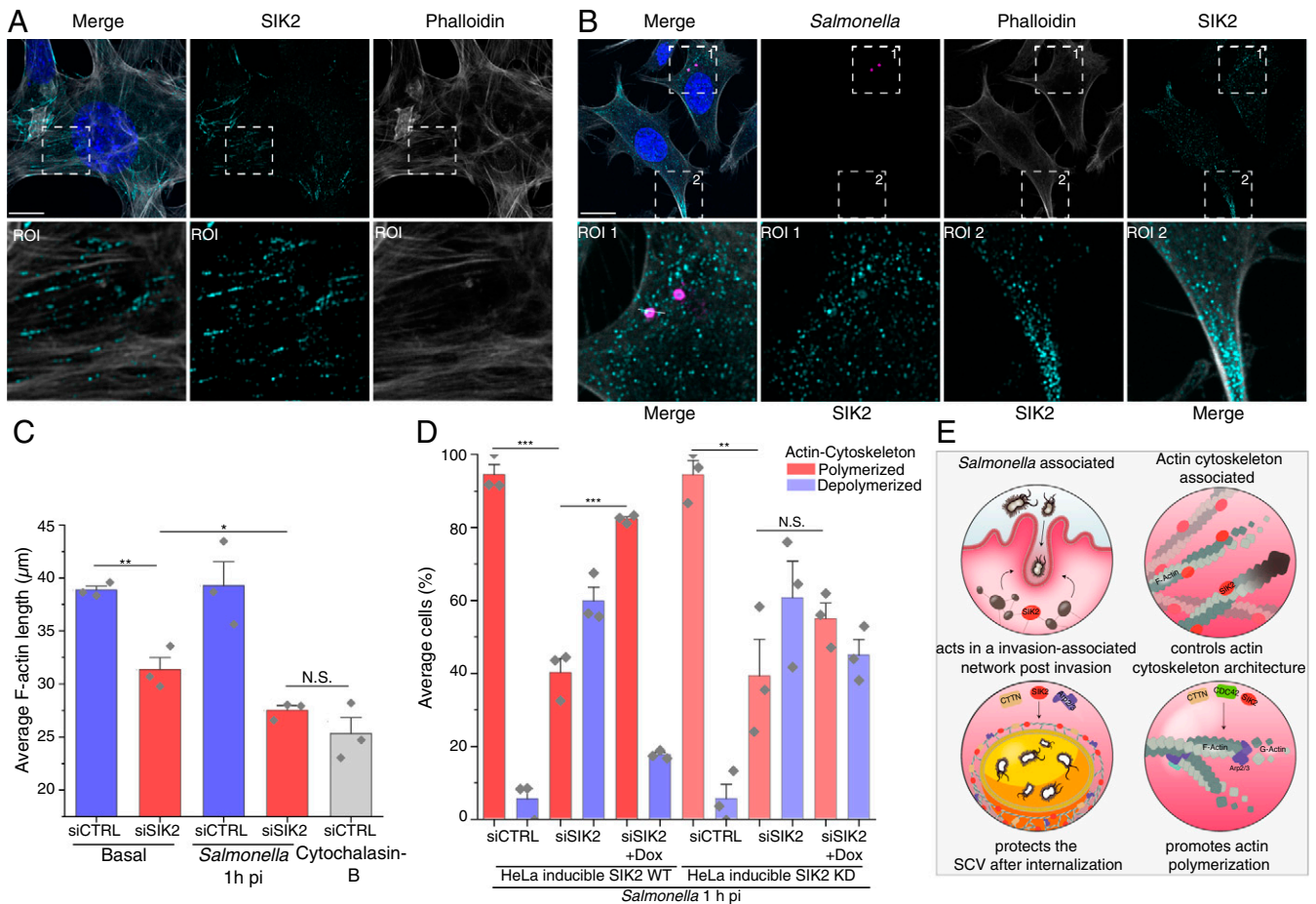


Fig. 5. SIK2 is required for the actin cytoskeleton integrity. (A) Immunofluorescence of MEFs stained for endogenous SIK2, Phalloidin, and DAPI. (B) Immunofluorescence of MEFs infected with *Salmonella* 30 min pi and stained for endogenous SIK2, *Salmonella* (anti-*Salmonella* CSA antibody), Phalloidin, and DAPI. (C) Quantification of Phalloidin-stained F-actin length. HeLa cells were siRNA transfected and infected with *Salmonella* 1 h pi and stained with Phalloidin, Tubulin, *Salmonella*, and DAPI and quantitatively analyzed. Cells transfected with control siRNA were treated with Cytochalasin B (2 µM) for 30 min where indicated. Data presented as mean + SEM, $n = 3$, > 500 cell counts per condition, $**P \leq 0.01$, and $*P \leq 0.05$ as analyzed by Student's *t* test. (D) Quantification of phenotypic analysis of cells showing defective actin polymerization. HeLa cells expressing HA-SIK2 wild type or SIK2 K49A under a doxycycline-inducible promoter were transfected with siCTRL or siSIK2, $^{-/-}$ doxycycline, and infected with *Salmonella* 1 h pi. Cells were stained with Phalloidin and DAPI and phenotypically analyzed by confocal microscopy. Data presented as mean + SEM, $n = 3$, 100 cell counts per condition, $***P \leq 0.001$, and $**P \leq 0.01$ as analyzed by Student's *t* test. (E) Proposed functions of SIK2 upon *Salmonella* infection. (A and B) Images are maximum intensity projections of confocal z-stacks. (Scale bar, 10 µm.)

stabilization factors. The Arp2/3 complex, Formins, type II myosins, IQGAP, and CDC42 are all required for the efficient *Salmonella* invasion (37, 44, 45). This event was not affected by SIK2 depletion. In contrast, we were able to demonstrate that SIK2 acts at a later stage of infection.

It is intriguing to recognize that SIK2 takes on a central role in the *Salmonella* invasion-associated network, in which it assumes a different function acting on the SCV postinvasion. This is supported by our findings, which show that SIK2 depletion is causing bacterial hyperproliferation rather than bacterial hyper- or hypo-invasion. SIK2 is recruited to the SCV shortly after the invasion, in which it colocalizes with the elements of the actin machinery. Based on our data, we propose a model of SIK2-induced actin de novo synthesis around the SCV, which may establish a protective shield to prevent the evasion of bacteria out of the SCV and into the cytosol or SCV fusion that may establish a larger intracellular compartment for bacterial proliferation. Furthermore, SIK2 depletion impairs fusion of the autolysosome with cytosolic bacteria. The combination of enhanced SCV escape into the cytosol and the impaired lysosomal degradation of cytosolic bacteria leads to a fatal cellular outcome, resulting into hyperproliferative *Salmonella*.

Strikingly, SIK2 is not acting exclusively on the local actin assembly associated with SCV but impacts the actin cytoskeleton architecture in its entirety (SI Appendix, Fig. S6). We demonstrated that SIK2 binds actin under the basal conditions and decorates filamentous actin in fibroblasts and in the areas undergoing rearrangements (e.g., Lamellipodia or actin stress fibers). In this process, FMNL2 (FHOD2) may represent, along with FHOD1, the second Formin playing a crucial role in *Salmonella* infection process (46). FMNL2 is critical for Lamellipodia and stress fiber formation and may act cooperatively with the Arp2/3 complex in the analogy to previous reports for other Formins (47, 48). SIK2 deletion results in reduction of filamentous actin, an effect which becomes even more pronounced upon *Salmonella* infection, resulting in a major defect in actin polymerization.

SIK2 is a central regulator/modulator of actin assembly and polymerization, with its role becoming most prominent upon *Salmonella* infection. Our work provides mechanistic insights into the regulation of the actin cytoskeleton and its role in controlling the acute *Salmonella* infection (Fig. 5E).

These results provide a solid foundation for the future work that will focus on understanding the molecular dynamics of the

protein–protein interaction, in order to precisely delineate and define the temporal regulation of the early SIK2-controlled events of the intracellular propagation of *Salmonella*. What remains to be defined are the direct substrates of SIK2 and how these substrate interactions relate to the observed, here described, effects on actin assembly/formation.

It is unknown whether SIK2 activation also protects against other intracellular intruders. Upon *Chlamydia* infection, the cytoskeletal network surrounding and stabilizing the bacterial vacuole hours after the invasion has been reported (49). After *Salmonella* infection, an actin meshwork around the SCV assembles in a SPI-2 (SteC)–dependent manner (≥ 6 h pi) (9–13). Here we report that SIK2 acts directly postinvasion in a SPI-1 (SopE)–dependent way to build up an actin shield around the SCV. In addition, the more recent work reported an analogous actin network, which builds up a cocoon-like actin structure after *Shigella* infection. The *Shigella*-triggered actin network (e.g., Arp2/3 complex, CDC42, and Cortactin) protects the bacterial vacuole and seems to function as a gatekeeper (50, 51). In contrast to *Salmonella*, *Shigella* actively destabilizes the SCV to help escape into the host cytosol <10 min pi (52, 53). It may be interesting to analyze the role of SIK2 upon *Shigella* infection and compare the sequence of molecular events in the early process pi between *Salmonella* and *Shigella*. This may help to obtain insights into potential targets valuable for therapeutic strategies and anti-bacterial defense of intracellular bacteria/parasites in general.

Studying the cellular host response to *Salmonella* infection identified SIK2 as a critical host defense kinase, which modulates a fundamental cellular process (e.g., F-actin polymerization) in a way that it limits intracellular proliferation of bacteria, may provide an exciting starting point for those future studies.

Materials and Methods

Bacterial Strains. *S. enterica* serovar Typhimurium strain SL1344 (gift from David Holden, Imperial College London), SL1344 Δ SPI-1 described earlier (54) (gift from Jorge Galan, Yale School of Medicine), SL1344 puHpT-GFP (SFH2) expressing GFP when exposed to the host cytosol, controlled by a glucose-6-phosphate-inducible promoter described earlier (27) (gift from Dirk Bumann, Biozentrum, University of Basel), and *S. Typhimurium* 12023 pFPV25.1-mCherry described earlier (55) (gift from Felix Randow, LMB) were used in this study.

Salmonella Culturing and Infections. Single *Salmonella* colonies were picked from a lysogeny broth (LB) Agar plate and inoculated into 1 mL LB medium (plus the respective antibiotic) and grown overnight to a stationary phase at 37 °C. Next day, *Salmonella* was diluted 1:33 and grown for 3.5 h at 37 °C before infection. Cells were infected in antibiotic-free medium with a multiplicity of infection of 100 for 10 min and washed afterward twice with phosphate-buffered saline (PBS). Subsequently, cells were cultured further in medium containing 100 μ g/mL Gentamycin for 1 h and thereafter reduced to 20 μ g/mL Gentamycin for the remaining time of the experiment.

Cell Lines. HeLa, HCT116, HEK293T, MEFs, and HeLa Flp-In T-Rex GFP-SopA or GFP-SopE [described earlier (56, 57)] were grown in Iscove's Modified Dulbecco's Media (IMDM) or Dulbecco's Modified Eagle Medium (DMEM), supplemented with 10% fetal calf serum (FCS) (heat-inactivated at 56 °C for 30 min) and 20 μ g/mL Gentamycin at 37 °C and 5% CO₂. All cell lines were routinely checked for mycoplasma infections using MycoAlert (Lonza). The cells were passaged two to three times a week and were used for experiments at passages between 2 to 35.

Colony-forming unit (CFU) Assay. HeLa cells were seeded in triplicates with 2×10^4 cells into a 24-well and siRNA-transfected in antibiotic-free medium. The experiment was performed 48 to 72 h posttransfection. After the infection, cells were washed with PBS and cultured with Gentamycin-containing medium. At 1, 6, or 8 h pi, cells were lysed in 0.1% (vol/vol) Triton X-100 in PBS and serial diluted in PBS. Diluted lysates were plated in technical duplicates on Agar plates and incubated for colony formation overnight at 37 °C. The number of colonies (within the linear range of the assay) was enumerated using a colony counter apparatus and software (aCOLyte 3, Synbiosis).

SDS-PAGE and Immunoblotting. Cells were washed twice with cold PBS and lysed in Lysis Buffer (50 mM Hepes, pH 7.5, 150 mM NaCl, 1 mM EDTA, 1 mM EGTA, 1% Triton X-100, 25 mM NaF, 5% glycerol, and 10 μ M ZnCl₂) or SDS Lysis Buffer (30 mM Tris-HCl, pH 7.4, 120 mM NaCl, 2 mM EDTA, 2 mM KCl, 0.5% CHAPS, 1% SDS, 50 mM NaF, and 5 mM Na₃VO₄) supplemented with complete protease inhibitors (cOmplete, EDTA-free; Roche Diagnostics) and phosphatase inhibitors (P5726, P0044; Sigma-Aldrich). Cell lysates were cleared by spinning at 20,000 g for 15 min at 4 °C in a centrifuge. Cell extracts were incubated with SDS sample buffer (50 mM Tris-HCl, pH 6.8, 10% glycerol, 2% SDS, 0.02% bromophenol blue, and 5% β -mercaptoethanol) and heated at 95 °C for 5 min. Samples were loaded onto 4 to 20% precast gradient Gels (BioRad) or self-casted 8% or 10% acrylamide gels and separated by SDS-PAGE. Proteins were probed by wet-transfer onto a Nitrocellulose or PVDF membrane and blocked with 5% low-fat milk or 5% bovine serum albumin (BSA) in Tris-buffered saline (TBS) (150 mM NaCl, 20 mM Tris, and pH 8.0) for 1 h. Primary antibodies were diluted in 5% BSA in TBS-T (TBS + 0.1% Tween 20) and secondary antibodies in 5% low-fat milk in TBS-T.

Protein Immunoprecipitation. Following cell lysis under nondenaturing conditions, cleared cell extracts were incubated with Lysis Buffer–equilibrated antibody-coupled resin. Therefore, HA agarose beads (Sigma-Aldrich) were used and incubated with lysates for 2 h at 4 °C on a rotating platform. Protein-bound beads were washed four times with Lysis Buffer. Immunoprecipitated and input samples were reduced in SDS sample buffer and heated at 95 °C for 5 min.

G-Actin/F-Actin Fractionation. G-actin and F-actin fractions were extracted from HeLa cell lysates by ultracentrifugation at 100,000 rpm using the G-actin/F-actin in vivo assay biochem kit (Cytoskeleton, Inc., BK037) according to the manufacture protocol. The levels of G-actin and F-actin were quantified by Western blotting using the anti-actin antibody provided in the kit.

Immunofluorescence, Confocal Microscopy. Cells were seeded on glass coverslips and washed after the treatment twice with PBS before fixation with 4% paraformaldehyde in PBS for 10 min. Cells were permeabilized with 0.2% (vol/vol) Triton X-100 in PBS for 10 min and blocked with 5% BSA in PBS for 1 h. Primary and secondary (including 4',6-diamidino-2-phenylindole [DAPI] and Phalloidin) antibodies were incubated in 5% BSA in PBS for 1 h with three PBS washes in between. Before mounting in Mowiol (Sigma), cells were washed three times and once with distilled water. Images were acquired on a Leica TCS SP8 microscope with a 63 \times oil immersion objective. For an automatic quantitative analysis, images were taken using the Yokogawa CQ1 confocal quantitative image cytometer platform (63 \times magnification). Cells were seeded onto black, clear flat-bottom 24-well plates and stained with indicated antibodies. The images were analyzed using the CQ1 Yokogawa CellPathfinder, high-content analysis software with the built-in plugin for cytoskeleton fiber detection. DAPI and Tubulin staining were used for determining the cell body of each cell.

CRISPR/Cas12-Assisted PCR Tagging. Endogenous tagging was performed as described (29) and on <http://www.pcr-tagging.com>. Briefly, the PCR cassette was amplified from pMaCTag-P27 (1 \times HA) plasmid in combination with M1_SIK2_fwd and M2_SIK2_AscP1_TATV_rev primer using a Velocity polymerase (Biolone) and High-Fidelity (HiFi) buffer (20 mM Tris-HCl, pH 8.8, 10 mM [NH₄]₂SO₄, 50 mM KCl, 0.1% [vol/vol] Triton X-100, 0.1 mg/mL BSA, and 2 mM MgCl₂) on a gradient PCR cyclor. The PCR product was gel purified with GeneJET Gel Extraction Kit. HeLa cells were transiently transfected with 1 μ g of the PCR cassette and 1 μ g pcDNA3.1-hAsCpf1(TATV) (pY220) using GeneJuice (Merck Millipore) according to the manufacture protocol and selected with 0.5 μ g/mL Puromycin 72 h posttransfection.

Lentiviral Transduction and Cell Line Generation. HEK293T cells were cotransfected with the lentiviral plasmid (pLTD N-term HA cloned with SIK2 WT or SIK2 K49A) together with the packaging vectors pPAX2 and pMD2. The medium containing the lentivirus was exchanged after 24 h, and after another 24 h, medium was collected for transduction of the recipient cells. Recipient cells were transduced with 1 mL of the virus containing medium with polybrene (8 μ g/mL; Sigma-Aldrich, H9268-5G). Cells were selected 48 h posttransduction with 1 μ g/mL Puromycin.

RNA Interference. Cells were transfected 24 h postseeding with 20nM siRNA (ON TARGETplus anti-SIK2 siRNA [Horizon Discovery] and AllStars Negative Control siRNA [Qiagen]) using Lipofectamine RNAiMAX (Life Technologies) according to the manufacture protocol. Experiments were performed 48 to

72 h posttransfection. Transfection efficiency was verified by Western blotting.

Phos-Tag Gels. Phos-tag acrylamide (Wako) gels were prepared and used according to manufactures protocol. Gels were prepared with 6% acrylamide, 25 μ M Phos-tag reagent, and 100 μ M MnCl₂. Cells were lysed in SDS Lysis Buffer.

SILAC-Based Phosphoproteomics. HCT116 cells were grown in SILAC-DMEM (arginine and lysine-free medium), supplemented with dialyzed FCS (10%) and lysine (74 μ g/mL) and arginine (42 μ g/mL) as "light K0, R0," "medium K4, R6," or "heavy K8, R10." Cells were lysed in 6 M Guanidinium hydrochloride (100 mM Tris HCl pH 8.5, 5 mM TCEP, and 10 mM chloracetamide), heated at 95 °C for 15 min, and sonicated with Sonics Vibra-Cell (1 s ON/1 s OFF pulse for 30 s using 30% amplitude). Phosphoproteomic analysis was performed as previously described (58). The cell lysates were diluted to 2 M guanidium hydrochloride with 50 mM Hepes buffer at pH 8.5 and incubated with Lys-C (1 μ g for 100 μ g protein lysate) for 2 h followed by further dilution to 1 M guanidium hydrochloride and overnight digestion with Trypsin (1 μ g for 100 μ g protein lysate). Peptides were desalted and quantified using bicinchoninic acid assay (BCA) assay. Equal peptide amounts from the three SILAC states were mixed at 1:1:1 ratio and dried down. This was followed by fractionation on a high-pH gradient into a total of 12 fractions. TiO₂-based phospho-enrichment was performed, followed by data acquisition on a Q Exactive HF instrument.

TMT Labeling. After tryptic digestion peptides were cleaned up using Sep-Pak tC18 (Waters, 50 mg) according to the manufactures protocol. Peptides were resuspended into TMT-labeling buffer (0.2 M EPPS pH8.2 and 10% Acetonitrile) and peptide concentration determined by μ BCA-assay (Thermo Fisher Scientific). Peptides were labeled with a 1:2 ratio (1mg peptide and 2 mg TMT reagent) with TMT reagents (Thermo Fisher Scientific, 90110 and A44520) for 1 h at room temperature (RT). The reaction was quenched with 0.5% (final concentration) hydroxylamine for 15 min at RT. Samples were multiplexed with equimolar ratios (unless stated otherwise) and cleaned up using Empore C18 (Octadecyl) resin material (3M Empore) as described earlier (59).

TMT-Based Phosphoproteomics. HeLa cells were lysed in (2% SDS, 50 mM Tris-HCl pH8, 150 mM NaCl, 10 mM TCEP, and 40 mM chloracetamide), heated at 95 °C for 10 min, and sonicated with Sonics Vibra-Cell (1 s ON/1 s OFF pulse for 30 s using 30% amplitude). Protein lysates were precipitated by methanol/chloroform using four volumes of ice-cold methanol, one volume of chloroform, and three volumes of water. The mixture was centrifuged at 20,000 g for 30 min, and the upper aqueous phase was removed and three volumes of ice-cold methanol added. Proteins were pelleted by centrifugation and washed twice with one volume of ice-cold methanol and air dried. The resulting protein pellet was resuspended in 8 M urea with 10 mM EPPS pH 8.2. Protein concentration was determined by Bradford assay. For digestion, 300 μ g proteins were diluted to 1 M urea and incubated 1:50 with LysC (Wako Chemicals) for 3 h and 1:100 with sequencing grade trypsin (Promega) overnight. The reaction was acidified using TFA (0.5%) and purified using Sep-Pak tC18 (Waters, 50 mg) according to manufacturer's protocol. A total 100 μ g of peptides were TMT labeled and channels adjusted to equimolar ratios as judged by single-injection measurements by liquid chromatography (LC)-mass spectrometry (MS). Ratio-adjusted peptides were multiplexed and used for phosphopeptide enrichment using High-Select Fe-NTA Phosphopeptide Enrichment Kit (Thermo Fisher Scientific) according to manufactures protocol. Phosphopeptides were cleaned up by C8 stage tip and fractionated using C18 stage tips. After washing (80% acetonitrile) and equilibration step with 0.1% TFA, peptides were loaded on C18 stage tips in 0.1% TFA solution and washed twice with 0.1% TFA in water. Peptides were fractionated into 16 fractions with an acetonitrile gradient from 2.5 to 50% in 0.1% Triethylamine and cross-concatenated into eight fractions. Samples were vacuum dried for LC-MS measurements.

HA-IP, On-Bead Digest, and TMT Labeling. Cells were lysed in 1% Triton X-100-based Lysis Buffer and incubated with HA agarose beads (Sigma) for 2 h at 4 °C on a rotating platform. Protein-bound beads were washed three times with Lysis Buffer and three times with Lysis Buffer without detergents. Samples were incubated with 25 μ l SDC buffer (2% sodium deoxycholate [SDC], 1 mM TCEP, 4 mM chloracetamide, and 50 mM Tris pH 8.5) and heated at 95 °C for 10 min. Samples were mixed 1:1 with 500 ng LysC and 500 ng Trypsin (50 mM Tris and pH 8.5) and digested overnight at 37 °C. Reaction was stopped with 150 μ l of isopropanol with 1% TFA. Peptides were cleaned up by loading them onto styrenedivinylbenzene-reverse phase sulfonate (SDB-RPS) (Empore) stage tips. After one wash with 1% TFA in isopropanol and one wash with 0.2% TFA in

water, peptides were eluted using 80% acetonitrile and 1.25% ammonia. Eluted peptides were dried, TMT labeled, and processed for LC-MS measurements.

Liquid Chromatography MS. For Q Exactive HF: Peptides were separated on an easy nLC 1200 (Thermo Fisher) and a 15 cm long, 75 μ m inner diameter (ID)-fused silica column, which has been packed in house with 1.9 μ m C18 particles (ReproSil-Pur, Dr. Maisch), and kept at 45 °C using an integrated column oven (Sonation). Peptides were eluted by linear gradient from 5 to 38% acetonitrile over 120 min and directly sprayed into a Q Exactive HF mass spectrometer equipped with a nanoFlex ion source (Thermo Fisher Scientific) at a spray voltage of 2.3 kV. Full-scan MS spectra (350 to 1,400 m/z) were acquired at a resolution of 120,000 at m/z 200, a maximum injection time of 100 ms and an automatic gain control (AGC) target value of 3×10^6 charges. Up to 10 most intense peptides per full scan were isolated using a 1 Th window and fragmented using higher-energy collisional dissociation (normalized collision energy of 35). MS/MS spectra were acquired with a resolution of 60,000 at m/z 200, a maximum injection time of 128 ms, and an AGC target value of 1×10^5 . Ions with charge states of 1 and >6 as well as ions with unassigned charge states were not considered for fragmentation. Dynamic exclusion was set to 20 s to minimize repeated sequencing of already acquired precursors. Enriched phosphopeptides were analyzed on a Q Exactive HF instrument coupled to nLC 1200. A 15 cm column was used as described above. For SILAC phosphoproteome analysis, the MS parameters are as follows: MS1: 60,000 resolution, AGC: 3e6, and injection time: 20 ms and MS2: resolution: 30,000, AGC: 1e5, injection time: 110 ms, and TOP N: 12.

Data were acquired in centroid mode on an Orbitrap Fusion Lumos mass spectrometer hyphenated to an easy nLC 1200 nano high-performance liquid chromatography (HPLC) system using a nanoFlex ion source (Thermo Fisher Scientific) applying a spray voltage of 2.6 kV with the transfer tube heated to 300 °C and a funnel radio frequency (RF) of 30%. Internal mass calibration was enabled (lock mass 445.12003 m/z). Peptides were separated on a self-made, 32 cm long, 75 μ m ID-fused silica column, packed in house with 1.9 μ m C18 particles (ReproSil-Pur, Dr. Maisch), and heated to 50 °C using an integrated column oven (Sonation). HPLC solvents consisted of 0.1% formic acid in water (Buffer A) and 0.1% formic acid, 80% acetonitrile in water (Buffer B). For phosphopeptide analysis, each peptide fraction was eluted by a linear gradient from 5 to 32% B over 120 min followed by a step-wise increase to 95% B in 8 min which was held for another 7 min. Full-scan MS spectra (350 to 1,400 m/z) were acquired with a resolution of 120,000 at m/z 200, maximum injection time of 100 ms, and AGC target value of 4×10^5 . The 20 most intense precursors per full scan with a charge state between 2 and 5 were selected for fragmentation ("Top 20"), isolated with a quadrupole isolation window of 0.7 Th, and fragmented via high energy collision-induced dissociation (HCD) applying a normalized collision energy (NCE) of 38%. MS2 scans were performed in the Orbitrap using a resolution of 50,000 at m/z 200, maximum injection time of 86 ms, and AGC target value of 1×10^5 . Repeated sequencing of already-acquired precursors was limited by setting a dynamic exclusion of 60 s and 7 ppm, and advanced peak determination was deactivated.

MS Data Analysis. Raw files were analyzed using Proteome Discoverer (PD) 2.4 software (Thermo Fisher Scientific). Spectra were selected using default settings and database searches performed using SequestHT node in PD. Database searches were performed against trypsin-digested Homo Sapiens SwissProt database and *Salmonella typhimurium* (strain LT2/SGSC1412/ATCC 700720) database. Static modifications were set as TMT6 at the N terminus and lysines and carbamidomethyl at cysteine residues. Search was performed using Sequest HT taking the following dynamic modifications into account: Oxidation (M), Phospho (S,T,Y), Met-loss (N-term), Acetyl (N-term), and Met-loss acetyl (N-term). For whole-cell proteomics, the same settings were used, except phosphorylation was not allowed as dynamic modification. For phosphoproteomics, all peptide groups were normalized by summed intensity normalization and then analyzed on peptide level. For whole-cell proteomics, normalized peptide-spectrum matches (PSMs) were summed for each accession and data exported for further use. For SILAC phosphoproteomics data, MaxQuant was used with default SILAC parameters. Methionine oxidation, N-terminal acetylation, and phosphorylation (pSTY) were used as the variable modifications.

Significance Testing. Statistical significance was assessed with two-sided Student's *t* test. *P* values ≤ 0.05 were considered as significant. Adjusted *P* values were corrected by Benjamini-Hochberg false discovery rate (FDR). Differences with *P* ≤ 0.05 are annotated as **P* ≤ 0.01 , ***P* ≤ 0.01 , and ****P* ≤ 0.001 . *P* > 0.05 are annotated N.S. (not significant) Data are presented as the mean of replicates with error bars indicating the SD or SEM. For clustering and enrichment analyses (see below), q-value cutoffs of 0.001 were used for significance definition. N represents number of independent replicates.

Hierarchical Clustering. Hierarchical cluster analysis was performed using Perseus software (version 1.6.5.0) with default settings after centering and scaling of data (z-scores).

Interaction Network and Pathway Enrichment Analysis. Identified genes were analyzed with Cytoscape with plugins for ReactomeFI, STRING, and Omics-Visualizer. Pathway enrichment analysis was performed by ReactomeFI Cytoscape plugin. Networks were generated with ReactomeFI or STRING (confidence cutoff of 0.9), as indicated.

Data Availability. The MS proteomics data have been deposited to the ProteomeXchange Consortium via the PRIDE (60) partner repository (<https://www.ebi.ac.uk/pride/archive>) with the dataset identifier PXD023703 (Fig. 1) and PXD021859 (Figs. 3 and 4).

1. S. E. Majowicz *et al.*; International Collaboration on Enteric Disease 'Burden of Illness' Studies, The global burden of nontyphoidal *Salmonella* gastroenteritis. *Clin. Infect. Dis.* **50**, 882–889 (2010).
2. L. A. Knodler, J. R. Elfenbein, *Salmonella enterica*. *Trends Microbiol.* **27**, 964–965 (2019).
3. J. E. Galán, *Salmonella* interactions with host cells: Type III secretion at work. *Annu. Rev. Cell Dev. Biol.* **17**, 53–86 (2001).
4. P. Cossart, P. J. Sansonetti, Bacterial invasion: The paradigms of Enteroinvasive pathogens. *Science* **304**, 242–248 (2004).
5. F. Randow, J. D. MacMicking, L. C. James, Cellular self-defense: How cell-autonomous immunity protects against pathogens. *Science* **340**, 701–706 (2013).
6. R. C. Orchard, N. M. Alto, Mimicking GEFs: A common theme for bacterial pathogens. *Cell. Microbiol.* **14**, 10–18 (2012).
7. W.-D. Hardt, L.-M. Chen, K. E. Schuebel, X. R. Bustelo, J. E. Galán, *S. typhimurium* encodes an activator of Rho GTPases that induces membrane ruffling and nuclear responses in host cells. *Cell* **93**, 815–826 (1998).
8. S. J. Winder, K. R. Ayscough, Actin-binding proteins. *J. Cell Sci.* **118**, 651–654 (2005).
9. S. Méresse *et al.*, Remodelling of the actin cytoskeleton is essential for replication of intracellular *Salmonella*. *Cell. Microbiol.* **3**, 567–577 (2001).
10. K. E. Unsworth, M. Way, M. McNiven, L. Machesky, D. W. Holden, Analysis of the mechanisms of *Salmonella*-induced actin assembly during invasion of host cells and intracellular replication. *Cell. Microbiol.* **6**, 1041–1055 (2004).
11. J. A. Wasylanka *et al.*, Role for myosin II in regulating positioning of *Salmonella*-containing vacuoles and intracellular replication. *Infect. Immun.* **76**, 2722–2735 (2008).
12. C. Odendall *et al.*, The *Salmonella* kinase SteC targets the MAP kinase MEK to regulate the host actin cytoskeleton. *Cell Host Microbe* **12**, 657–668 (2012).
13. J. Poh *et al.*, SteC is a *Salmonella* kinase required for SPI-2-dependent F-actin remodelling. *Cell. Microbiol.* **10**, 20–30 (2008).
14. Z. Wang, H. Takemori, S. K. Halder, Y. Nonaka, M. Okamoto, Cloning of a novel kinase (SIK) of the SNF1/AMPK family from high salt diet-treated rat adrenal. *FEBS Lett.* **453**, 135–139 (1999).
15. J. M. Lizcano *et al.*, LKB1 is a master kinase that activates 13 kinases of the AMPK subfamily, including MARK/PAR-1. *EMBO J.* **23**, 833–843 (2004).
16. F. Chen, L. Chen, Q. Qin, X. Sun, Salt-inducible kinase 2: An oncogenic signal transmitter and potential target for cancer therapy. *Front. Oncol.* **9**, 18 (2019).
17. K. Sakamoto, L. Bultot, O. Göransson, The salt-inducible kinases: Emerging metabolic regulators. *Trends Endocrinol. Metab.* **29**, 827–840 (2018).
18. J. Sakamaki *et al.*, Role of the SIK2-p35-PJA2 complex in pancreatic β -cell functional compensation. *Nat. Cell Biol.* **16**, 234–244 (2014).
19. E. Fiskin, T. Bionda, I. Dikic, C. Behrends, Global analysis of host and bacterial ubiquitinome in response to *Salmonella typhimurium* infection. *Mol. Cell* **62**, 967–981 (2016).
20. J. C. Patel, J. E. Galán, Differential activation and function of Rho GTPases during *Salmonella*-host cell interactions. *J. Cell Biol.* **175**, 453–463 (2006).
21. A. M. Keestra *et al.*, Manipulation of small Rho GTPases is a pathogen-induced process detected by NOD1. *Nature* **496**, 233–237 (2013).
22. S. Mostoway, A. R. Shenoy, The cytoskeleton in cell-autonomous immunity: Structural determinants of host defence. *Nat. Rev. Immunol.* **15**, 559–573 (2015).
23. S. J. L. van Wijk *et al.*, Linear ubiquitination of cytosolic *Salmonella Typhimurium* activates NF- κ B and restricts bacterial proliferation. *Nat. Microbiol.* **2**, 17066 (2017).
24. J. Ninomiya-Tsuji *et al.*, The kinase TAK1 can activate the NIK-1 κ B as well as the MAP kinase cascade in the IL-1 signalling pathway. *Nature* **398**, 252–256 (1999).
25. W. Liu *et al.*, Activation of TGF- β -activated kinase 1 (TAK1) restricts *Salmonella Typhimurium* growth by inducing AMPK activation and autophagy. *Cell Death Dis.* **9**, 570 (2018).
26. C. L. Birmingham, A. C. Smith, M. A. Bakowski, T. Yoshimori, J. H. Brumell, Autophagy controls *Salmonella* infection in response to damage to the *Salmonella*-containing vacuole. *J. Biol. Chem.* **281**, 11374–11383 (2006).
27. M. Polajnar, M. S. Dietz, M. Heilemann, C. Behrends, Expanding the host cell ubiquitylation machinery targeting cytosolic *Salmonella*. *EMBO Rep.* **18**, 1572–1585 (2017).
28. O. Steele-Mortimer, The *salmonella*-containing vacuole: Moving with the times. *Curr. Opin. Microbiol.* **11**, 38–45 (2008).
29. J. Fueller *et al.*, CRISPR-Cas12a-assisted PCR tagging of mammalian genes. *J. Cell Biol.* **219**, 615 (2020).
30. K. G. Campellone, M. D. Welch, A nucleator arms race: Cellular control of actin assembly. *Nat. Rev. Mol. Cell Biol.* **11**, 237–251 (2010).
31. L. M. Machesky, S. J. Atkinson, C. Ampe, J. Vandekerckhove, T. D. Pollard, Purification of a cortical complex containing two unconventional actins from *Acanthamoeba* by affinity chromatography on profilin-agarose. *J. Cell Biol.* **127**, 107–115 (1994).

ACKNOWLEDGMENTS. We thank Karl-Richard Reuter for help with illustration work, Evgenij Fiskin for initial project support, Katarzyna Bogucka for providing protocols/reagents, and all members of the I.D. laboratory for support and constructive discussions. We thank Andrea Gubas for critical proofreading of the manuscript. We thank the q-Proteomics platform at the Institute of Biochemistry II (Frankfurt) for excellent support. Furthermore, we thank the Kraiczky laboratory (University Hospital of Frankfurt) for help with *Salmonella* work. This project has received funding from the European Research Council under the European Union's Horizon 2020 research and innovation program (Grant Agreement 742720), the grants from Else Kroener Fresenius Stiftung–Dr. Rolf M. Schwiete Stiftung, and was supported by the Deutsche Forschungsgemeinschaft (German Research Foundation) Projects 173096411–SPP 1580 and 259130777–SFB 1177. The Novo Nordisk Foundation Center for Protein Research is financially supported by the Novo Nordisk Foundation (NNF14CC0001).

32. R. D. Mullins, J. A. Heuser, T. D. Pollard, The interaction of Arp2/3 complex with actin: Nucleation, high affinity pointed end capping, and formation of branching networks of filaments. *Proc. Natl. Acad. Sci. U.S.A.* **95**, 6181–6186 (1998).
33. J. Block *et al.*, FMNL2 drives actin-based protrusion and migration downstream of Cdc42. *Curr. Biol.* **22**, 1005–1012 (2012).
34. S. Tojkander, G. Gateva, P. Lappalainen, Actin stress fibers—assembly, dynamics and biological roles. *J. Cell Sci.* **125**, 1855–1864 (2012).
35. P. Hotulainen, P. Lappalainen, Stress fibers are generated by two distinct actin assembly mechanisms in motile cells. *J. Cell Biol.* **173**, 383–394 (2006).
36. S. Vorwerk, V. Krieger, J. Deiwick, M. Hensel, N. Hansmeier, Proteomes of host cell membranes modified by intracellular activities of *Salmonella enterica*. *Mol. Cell. Proteomics* **14**, 81–92 (2015).
37. P. J. Hume, V. Singh, A. C. Davidson, V. Koronakis, Swiss army pathogen: The *Salmonella* entry toolkit. *Front. Cell. Infect. Microbiol.* **7**, 348 (2017).
38. S. Stender *et al.*, Identification of SopE2 from *Salmonella typhimurium*, a conserved guanine nucleotide exchange factor for Cdc42 of the host cell. *Mol. Microbiol.* **36**, 1206–1221 (2000).
39. D. Zhou, J. Galán, *Salmonella* entry into host cells: The work in concert of type III secreted effector proteins. *Microbes Infect.* **3**, 1293–1298 (2001).
40. D. Humphreys, A. Davidson, P. J. Hume, V. Koronakis, *Salmonella* virulence effector SopE and Host GEF ARNO cooperate to recruit and activate WAVE to trigger bacterial invasion. *Cell Host Microbe* **11**, 129–139 (2012).
41. R. D. Hayward, V. Koronakis, Direct nucleation and bundling of actin by the SipC protein of invasive *Salmonella*. *EMBO J.* **18**, 4926–4934 (1999).
42. E. J. McGhie, R. D. Hayward, V. Koronakis, Cooperation between actin-binding proteins of invasive *Salmonella*: SipA potentiates SipC nucleation and bundling of actin. *EMBO J.* **20**, 2131–2139 (2001).
43. Y. Fu, J. E. Galán, A *Salmonella* protein antagonizes Rac-1 and Cdc42 to mediate host-cell recovery after bacterial invasion. *Nature* **401**, 293–297 (1999).
44. J. Hänisch *et al.*, Activation of a RhoA/myosin II-dependent but Arp2/3 complex-independent pathway facilitates *Salmonella* invasion. *Cell Host Microbe* **9**, 273–285 (2011).
45. M. D. Brown, L. Bry, Z. Li, D. B. Sacks, IQGAP1 regulates *Salmonella* invasion through interactions with actin, Rac1, and Cdc42. *J. Biol. Chem.* **282**, 30265–30272 (2007).
46. D. Truong *et al.*, Formin-mediated actin polymerization promotes *Salmonella* invasion. *Cell. Microbiol.* **15**, 2051–2063 (2013).
47. K. Rottner, J. Faix, S. Bogdan, S. Linder, E. Kerkhoff, Actin assembly mechanisms at a glance. *J. Cell Sci.* **130**, 3427–3435 (2017).
48. S. Tojkander *et al.*, A molecular pathway for myosin II recruitment to stress fibers. *Curr. Biol.* **21**, 539–550 (2011).
49. Y. Kumar, R. H. Valdivia, Actin and intermediate filaments stabilize the *Chlamydia trachomatis* vacuole by forming dynamic structural scaffolds. *Cell Host Microbe* **4**, 159–169 (2008).
50. S. Ehsani *et al.*, Hierarchies of host factor dynamics at the entry site of *Shigella flexneri* during host cell invasion. *Infect. Immun.* **80**, 2548–2557 (2012).
51. S. Kühn *et al.*, Actin assembly around the *Shigella*-containing vacuole promotes successful infection. *Cell Rep.* **31**, 107638 (2020).
52. I. Paz *et al.*, Galectin-3, a marker for vacuole lysis by invasive pathogens. *Cell. Microbiol.* **12**, 530–544 (2010).
53. N. Mellouk, J. Enninga, Cytosolic access of intracellular bacterial pathogens: The *Shigella* paradigm. *Front. Cell. Infect. Microbiol.* **6**, 35 (2016).
54. V. M. Bruno *et al.*, *Salmonella Typhimurium* type III secretion effectors stimulate innate immune responses in cultured epithelial cells. *PLoS Pathog.* **5**, e1000538 (2009).
55. B. J. Ravenhill *et al.*, The cargo receptor NDP52 initiates selective autophagy by recruiting the ULK complex to cytosol-invading bacteria. *Mol. Cell* **74**, 320–329.e6 (2019).
56. E. Fiskin *et al.*, Structural basis for the recognition and degradation of host TRIM proteins by *Salmonella* effector SopA. *Nat. Commun.* **8**, 14004 (2017).
57. K. E. Yuki *et al.*, CYRI/FAM49B negatively regulates RAC1-driven cytoskeletal remodeling and protects against bacterial infection. *Nat. Microbiol.* **4**, 1516–1531 (2019).
58. A. Camgoz *et al.*, STK3 is a therapeutic target for a subset of acute myeloid leukemias. *Oncotarget* **9**, 25458–25473 (2018).
59. J. Rappsilber, M. Mann, Y. Ishihama, Protocol for micro-purification, enrichment, pre-fractionation and storage of peptides for proteomics using StageTips. *Nat. Protoc.* **2**, 1896–1906 (2007).
60. Y. Perez-Riverol *et al.*, The PRIDE database and related tools and resources in 2019: Improving support for quantification data. *Nucleic Acids Res.* **47**, D442–D450 (2019).